Star Formation Rates of Star Forming Galaxies in the Extended Groth Strip

Pranav Kukreti

A dissertation submitted for the partial fulfilment of BS-MS Dual Degree in Science

Indian Institute of Science Education and Research Mohali
April 2018

Certificate of Examination

This is to certify that the dissertation titled **Star Formation Rates of Star Forming Galaxies in the Extended Groth Strip** submitted by **Pranav Kukreti** (Reg. No. MS13100) for the partial fulfillment of BS-MS Dual Degree programme of the institute, has been examined by the thesis committee duly appointed by the institute. The committee finds the work done by the candidate satisfactory and recommends that the report be accepted.

Dr. Smriti Mahajan Dr. Harvinder K. Jassal Prof. Jasjeet S. Bagla
(Supervisor)

Dated: April 19, 2018

Declaration

The work presented in this dissertation has been carried out by me under the guidance of Prof. Jasjeet Singh Bagla at the Indian Institute of Science Education and Research, Mohali.

This work has not been submitted in part or in full for a degree, a diploma, or a fellowship to any other university or institute. Whenever contributions of others are involved, every effort is made to indicate this clearly, with due acknowledgement of collaborative research and discussions. This thesis is a bonafide record of original work done by me and all sources listed within have been detailed in the bibliography.

Pranav Kukreti
(Candidate)

Dated: April 19, 2018

In my capacity as the supervisor of the candidates project work, I certify that the above statements by the candidate are true to the best of my knowledge.

Prof. Jasjeet Singh Bagla
(Supervisor)

Acknowledgment

I would like to thank my supervisor, Prof. Jasjeet Singh Bagla, for letting me work with him on various projects throughout my time at IISER Mohali. His clarity of thought and a positive attitude towards every problem that we encountered have made this project and all the others before this, possible. A summer project with Nissim Kanekar in 2017 has been one of the major learning experiences of my academic life so far. It was not only the problem solving skills I learnt from him, but also how to identify problems worth solving. I would like to thank him for letting me bug him with questions throughout my final year. Apurba Bera has made essential contributions to this project by providing the stacking codes and showing the patience to help me out whenever I got stuck in the programmes and I thank him for this.

I would like to thank Saurav Shekhar for not murdering me for the endless number of questions I bothered him with and Sanjay Anand for taking out the time to do nothing together, which I have now come to realize, is crucial for my well being. Harshavardhan Thyagarajan has been an equal participant in almost every memorable experience (good and bad) in my time at IISER Mohali and I would like to thank him for that. I would also like to thank Suhani Gupta for always being up for a few minutes of whining over a cup of coffee and Alkit Gugalia for all the football games we've watched together.

Last, but by no measure the least, my parents, who have constantly supported me so that I could do what I wanted (although I'm still not sure they really understand what I do). Now that I think about it, I realize that I can never manage to thank them in a sentence or two, but I'm glad to have them by my side.

List of Figures

Abstract

Galaxy formation and evolution is an important open astrophysical problem in modern cosmology. Optical and Infrared studies of the deep fields (the Groth Strip, the Subaru Deep field, COSMOS etc) have helped make huge advancements in the understanding of galaxy formation and evolution. Probing star formation in galaxies at different redshifts helps to trace the amount of gas being converted to stars at different points of time, which is an important aspect of galaxy evolution. Most of the studies use ultraviolet/infrared/optical spectral lines, e.g., OII, OIII, Hα lines, or continuum emission, e.g., U band flux, as probes for star formation in galaxies. These probes are susceptible to dust attenuation because of the dust present in the source galaxy, the inter stellar medium, the inter galactic medium and the Milky Way. The extinction due to dust leads to an under estimation of the star formation rate. Although the re-emission by dust in the Infrared region can be used to estimate the total star formation rate (SFR), this requires the knowledge of the wavelength dependent dust attenuation factor, which is poorly known. However, multiwavelength studies of galaxies have been done and have given interesting results on star formation, dust attenuation and galaxy evolution.

Emission in the radio window from these galaxies is unaffected by dust. The non-thermal emission from normal galaxies is synchrotron radiation from relativistic electrons and thermal emission is free-free emission from HII regions. The emission in the radio window in normal galaxies is not dominated by stellar populations older than 100 million years. This means that radio emission gives an estimate of the recent star formation rate, whatever be the history of star formation in the galaxy. These reasons make radio emission an excellent probe to study star formation in galaxies as an unobscured estimator. The rest frame 1.4 GHz luminosity has been found to have a tight correlation with infrared luminosity ([1]), holding up to z$\sim$4, which can be used to estimate the star formation rate in intermediate to high redshift galaxies in a way unaffected by the dust. However, at intermediate to high redshifts, the emission from these galaxies is too faint for these galaxies to be detected individually with sensitivity of present day radio telescopes. To study the emission from such sources, a stacking analysis of the sources has to be used, which pushes the sensitivity levels way below the ones achievable by present day radio telescopes for direct imaging. The information obtained by stacking analysis is statistical in nature, but since we are interested in studying the behavior of typical star forming galaxies and not individual galaxies, this is not a heavy price to pay.

For our analysis I have made a deep continuum L band image of the Extended Groth Strip (EGS) at 1.4GHz in AIPS, using 57 hours of on-source data from Giant Meterwave Radio Telescope (GMRT), India under the supervision of Prof. Jasjeet Singh Bagla at IISER, Mohali, India. This data is a subset of the data taken with GMRT for the study of HI 21 cm emission from galaxies at z<0.4 in the EGS, being undertaken by Prof. Nissim Kanekar (NCRA-TIFR, Pune), Prof. Jayaram Chengalur (NCRA-TIFR, Pune) and Prof. Jasjeet Singh Bagla (IISER Mohali).I would also like to point out in passing that there is still no deep low-frequency radio continuum image of the EGS, since the best present VLA 1.4 GHz image of this field has a RMS noise of 20 μJy/Bm ([2]) which is far more than the other extra-galactic deep fields. We have used a radio stacking analysis to study the behavior of star formation rate of the typical star forming galaxies up to z = 1.4 in the EGS. The sources to be used for stacking were identified using the DEEP2 survey catalogue ([12]). The current analysis that we have done is for the GSB data with a bandwidth of 32 MHz.

With the stacking analysis we have studied the behavior of median total SFR and specific SFR with redshift, colour and stellar mass. We have also studied the behavior of dust extinction as a function of redshift, stellar mass and colour.

Contents

Chapter 1

1.1 Introduction I

Karl Jansky first detected radio emission from the Milky Way while looking for static with his "merry-go-round" antenna and since then, radio astronomy has made several important contributions to the understanding of various phenomena in the Universe. These discoveries include the HI 21cm emission from neutral Hydrogen, quasars, pulsars and the cosmic microwave background radiation, to name a few. Although objects in the universe emit radiation over the entire electromagnetic spectrum, when it comes to the radio window, there are certain factors that make it favorable for study. Earth's atmosphere is (almost) opaque to a major portion of the electromagnetic spectrum, which includes bands like Gamma ray, X-ray, UV and most of the infrared. Broadly, visible and radio emission are the two bands that are observable from the Earth. At wavelengths greater than a few meters, the ionosphere greatly limits the transmission of the radio waves. There are also some short windows in the infrared wavelengths which can be used for ground based observations. At these wavelengths the ground based telescopes can be used to study the universe with high resolution. Observations in the other bands require space based telescopes which are expensive to maintain. Although single-dish optical and infrared telescopes can provide a better resolution than single-dish radio telescopes, the inception of radio interferometers has made radio observations comparable to the arcsecond resolution of the optical and infrared counterparts. Combined with their wide field of view, radio interferometers have proven to be extremely useful for studying things like the dust-unobscured star formation in the high redshift universe.

1.1.1 Brightness temperature

In radio astronomy, a measure of flux S is used which is defined as -

$$S = \frac{dE}{dt}\frac{1}{A} \tag{1.1}$$

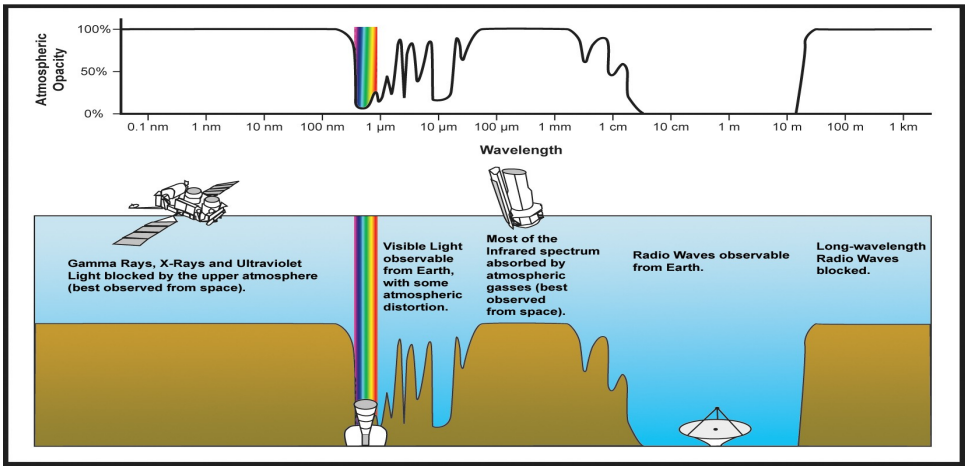

Figure 1.1: Atmospheric opacity for various bands in the EM spectrum. (source : Wikimedia commons)

where, E is the amount of energy that crosses the area A perpendicular to the direction of propagation. The flux is observed over a frequency band (flux density) and the total flux observed is calculated by integrating the flux over frequency. This flux density is measured in the units of Jansky (Jy) where 1 Jy = $10^{-26} W m^{-2} Hz^{-1}$. For extended sources, the flux density is described using the energy received per unit solid angle as well, so the units are $W m^{-2} Hz^{-1} sr^{-1}$. This is called the brightness (B) of the object.

If the object in the sky emitting the radiation is a black body, then the radiation can be described using Planck's formula for emission from a black body at temperature T -

$$B(\lambda, T) = \frac{2hc^2}{\lambda^5}\frac{1}{e^{\frac{hc}{\lambda kT}} - 1} \tag{1.2}$$

For radio waves, which fall in the long wavelength regime ($\lambda >>$ hc/KT), the exponential term in this Planck's equation can be expanded using the Taylor series

as -

$$\frac{1}{e^{\frac{hc}{\lambda kT}} - 1} \approx \lambda kT \tag{1.3}$$

Putting this in Planck's equation yields -

$$B(\lambda, T) = \frac{2ckT}{\lambda^4} \tag{1.4}$$

This is called the Rayleigh-Jeans approximation of Planck's law. The spectral brightness can also be written as -

$$B(\nu, T) = \frac{2kT}{\lambda^2} \tag{1.5}$$

This approximation can be used to write the temperature T as

$$T = \frac{\lambda^2 B(\nu)}{2k} \tag{1.6}$$

T is the brightness temperature, which is defined as the hypothetical temperature at which the body would have to be, assuming it is a black body, to produce the observed brightness at frequency ν.

The radio emission (upto $\nu \approx 200$ GHz) from normal galaxies is mostly either due to the thermal bremsstrahlung emission or the synchrotron emission. Thermal bremsstrahlung emission is produced by free electrons scattered by ions without being captured, generally from the HII regions. The brightness temperature for such emission regions is related to their physical temperature. On the other hand, synchrotron emission dominated sources do not have a black body spectrum, their flux increases with the observation wavelength. This is called the steep spectrum and for low frequencies, it can be written as $S_\nu \propto \nu^{-\alpha}$, where α is the spectral index and its typical value is 0.8 at long wavelengths ([4]). The brightness temperature is not a good approximation of the physical temperature in this case. This emission is also referred to as the non-thermal emission.

1.1.2 Antenna properties

An important parameter for antenna is its effective area. Assuming that an incoming plane wave intercepted by the antenna has a flux density S and the power extracted

by the antenna from it is P_{ext}, the effective area A_{eff} is defined as -

$$A_{eff} = \frac{P_{ext}}{S} \tag{1.7}$$

A_{eff} has the dimensions of m^2. Along with the geometric area A_{geo} of the antenna, A_{eff} can be used to define the aperture efficiency η_{ap} as

$$\eta_{ap} = \frac{A_{eff}}{A_{geo}} \tag{1.8}$$

The antennas of radio telescopes are direction sensitive, i.e. they are more sensitive to radiation incoming from certain direction than other directions. This direction sensitivity can be described by the power pattern, $P(\theta, \phi)$, of the antenna, which can be obtained using the effective area of the antenna and the maximum effective area as -

$$P(\theta, \phi) = \frac{A_{eff}(\theta, \phi)}{A_{eff}(max)} \tag{1.9}$$

Antennas follow the principle of reciprocity, which is useful in solving for the power pattern of an antenna. It states that the transmitting and receiving sensitivity of an antenna are same in any direction. This is helpful in obtaining the power pattern of the antenna, where now the electric field generated in a direction can be normalized to give the power pattern. A 3 dimensional figure of the power pattern is shown in Figure 2. The antenna has maximum sensitivity in the main lobe, where most of the radiation is contained. For the main lobe, the Half Power Beam Width (HPBW) is defined as the angular distance between the half power points of the main lobe, with respect to the central value. Some radiation is also contained in the side lobes of the pattern and the response to radiation goes to zero between any two lobes (null points). A better resolution is obtained by decreasing the HPBW and minimizing the response from the sidelobes to reduce the confusion in emission from the source. The HPBW can be expressed in terms of the observing wavelength and dish diameter as HPBW $\sim \frac{\lambda}{D}$. For instance, the HPBW of a single GMRT dish at $\lambda = 0.21$m is about 0.006 radians or 20.6 arcminutes. For GMRT, this is calculated for a 35m dish as the full 45m dish is not illuminated at this wavelength.

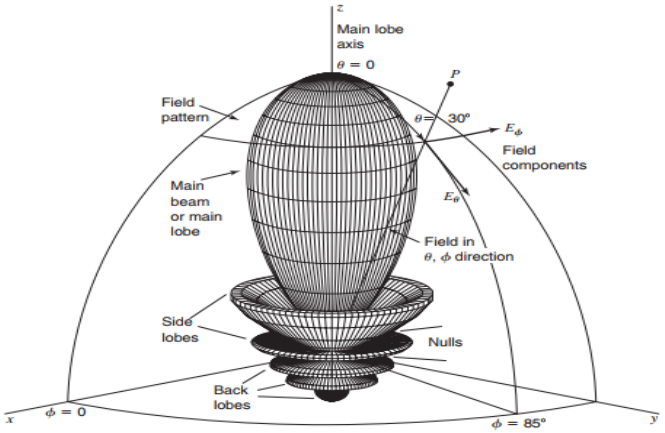

Figure 1.2: Three dimensional power pattern plot. The axis of the main lobe is aligned along the z axis and the direction of an arbitrary point P is shown with the electric field components at that point.

1.1.3 Subsystems of a Radio Telescope

The various subsystems of a radio telescope are shown in the block diagram below. The incoming electromagnetic waves generate voltages in the antenna terminal and these voltages vary with a frequency equal to that of the incoming wave. This is called the Radio Frequency (RF) [5]. The signal here is extremely weak and needs to be amplified. A Low Noise Amplifier (LNA) in the frontend is used at this stage to amplify the signal and making sure the amplifier adds as little noise to the signal as possible. This is necessary to observe really low temperature signals, for example, the cosmic microwave background radiation at 2.73 K. Such LNAs are maintained at low temperatures with cryogenic cooling so as to minimize thermal noise.

The next stage is that of the mixer. Radio signals are observed at different frequency bands from the same telescope and have to be transmitted from the antenna site to control rooms, which can be at long distances sometimes. Transferring the signals at their observed radio frequencies (RF) is not practically possible and cost efficient. The signal is therefore beat down to a lower frequency for transmission using the mixer. The mixer takes in input from the incoming signal and from a Local Oscillator (LO). This local oscillator is tunable and generally used to generate a pure sine wave. The output of the mixer is at the beat frequency of the LO frequency and RF frequency. The higher end of the frequency is stopped using a low pass filter.

The signal is now at a lower frequency than RF, called the Intermediate Frequency (IF). Transmission loss is a serious problem for telescopes and this is minimized by choosing suitable IFs. The signal is then amplified again by an amplifier and then

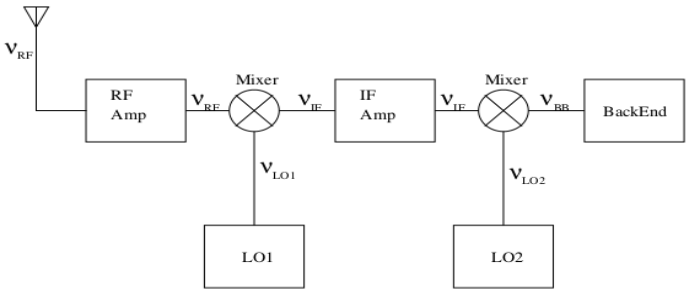

Figure 1.3: Block diagram of the basic subsystems involved in a single dish radio telescope. (source : *Low Frequency Radio Astronomy*, NCRA)

mixed again with a near 0 Hz signal. This is then transferred to the backend for processing.

Giant Meterwave Radio Telescope

The Giant Meterwave Radio Telescope (GMRT) is a radio interferometer located in Khodad, 80 km north of Pune, India. It consists of thirty 45m dishes spread over a maximum seperation of 25 km. It can observe in various frequency bands from 50 MHz to 1450 MHz with a bandwidth of upto 400 MHz. The GMRT has a hybrid configuration, with 14 antennas distributed randomly in the central square. The remaining antennas are placed along the three arms of a Y shape. The short baselines in the central square are useful in imaging large structures in the sky whereas the longer baselines are useful in observing sources with high angular resolution. At an observing frequency of 1.4 GHz, the synthesized beamwidth of the GMRT is about 1.8 arcseconds. The grid size of the mesh on a dish varies from 10 x 10 mm to 20 x 20 mm and that is why the actual dish diameter at 1.4 GHz is 35m, this is mainly due to the feed illuminating only the central part.

In a radio telescope, the system temperature T_{sys} is a measure of the total power available at the terminals of the telescope. When no source is being observed, the system temperature will just be the total noise in the system. The total noise is a sum of noises from different subsystems and have no correlation with each other. T_{sys} can therefore be written as -

$$T_{sys} = T_{sky} + T_{spill} + T_{rec} + T_{loss} \tag{1.10}$$

T_{sky} is the radiation received from the sky, even when the antenna is not pointing at a source. The sky contributes highly to low frequencies, but the cosmic microwave

Figure 1.4: Seven of the fourteen antennas in the central square (picture by Nissim Kanekar, NCRA-TIFR, Pune)

background radiation contributes 2.7K at all frequencies. The ground also re-radiates energy it has absorbed, which is picked up by the edges of the antenna. This noise is called the spillover noise T_{spill}. The receiver system also adds to the overall noise, T_{rec}, although the noise added by LNAs in the initial stages of amplification is usually insignificant. T_{loss} incorporates the noise added due to any lossy systems in the chain of subsystems.

The figure-of-merit for a radio antenna is the ratio of gain to system temperature, $\frac{G}{T_{sys}}$, which can be calculated as -

$$\frac{G}{T_{sys}} = \frac{SA_{geo}\eta_{ap}}{2kT_{sys}} \tag{1.11}$$

where S is the flux density in Jansky, A_{geo} is the geometrical area of the antenna and η_{ap} is the aperture efficiency. For the GMRT, at the observing frequency of 1.4GHz, the values of $\frac{G}{T_{sys}} = 3.17$ x 10^3 assuming a $T_{rec} = 308$K.

1.2 Introduction II

Making a complete picture of galaxy evolution, from the first stars in the universe to the present day galaxies with their diverse masses, sizes, colours, metallicities and luminosities, is still an open and one of the most difficult problems in modern astrophysics. Understanding star formation is key to understanding galaxy evolution. The picture at the moment hints that the star formation rate density peaked at $z \approx 2$ and then declined at an exponential rate ([6]). There are several tracers that can be used to probe star formation in galaxies, like the ultraviolet, infrared, sub-millimeter and radio emission and that is indeed the aim of many present day surveys; to use multi-wavelength data to make a complete picture of galaxy evolution upto high redshifts. The UV emission from galaxies is mostly from young short-lived massive stars, which means that it can be used to trace the instantaneous star formation rate density (SFRD). In dusty galaxies, the UV emission is largely absorbed by the interstellar dust and re-radiated at far infrared (FIR) wavelengths, so the FIR emission of such galaxies is a probe for young stellar populations and their SFRD. Solar-mass evolved stars in a galaxy are mostly responsible for the near infrared (NIR) emission and make up most of the stellar mass of the galaxy. The NIR emission can therefore be used to obtain the stellar mass density (SMD) of such galaxies. Emission line tracers like Hα, O[II] and O[III] from the excited gaseous regions of the galaxy are also good probes of the star formation rate.

Ideally, if there was no extinction, UV measurements would be a better way to trace star formation than infrared or radio. But the light coming from such galaxies faces severe dust extinction from dust grains present in the interstellar and intergalactic medium and so to get a complete picture of the star formation in such galaxies, it is necessary to use a combination of UV and IR/submm tracers. Emission in the long-wavelength regime is not absorbed by the interstellar or intergalactic dust but is extremely weak for high redshift galaxies. This faintness in signal makes it very hard to study such objects in the long wavelength regime. A point worth mentioning here is that the Atacama Large Millimeter/submillimeter Array (ALMA) will dramatically improve the detection limits of such faint galaxies at high redshifts. The Hubble Space Telescope Wide Field Camera 3 (HST WFC3) at NIR wavelengths has the imaging sensitivity to detect rest frame optical light upto $z < 3$. The Spitzer space telescope has a major upgrade in sensitivity and has detected luminous galaxies at $z \sim 8$. The James Webb Space Telescope (JWST) will improve the sensitivity and redshift limits

of such observations by an even greater amount.

The stellar population of galaxies have huge variations in mass, ages and metallicities. The spectra of galaxies are not enough to understand their various properties, generally, because they are a result of the composite stellar population whose true properties are unknown. For most of the galaxies, excluding the nearby ones, only the integrated spectra can be observed which are many times degenerate to the properties of the stellar population like metallicity, dust-attenuation, age etc. Therefore, certain assumptions are made to simplify the interpretation of the light. The initial mass function, relation between dust attenuation and wavelength, the star formation history of the galaxies and the metallicity distribution of the stellar population are some of the simplifying assumptions that can be made.

1.2.1 Initial Mass Function

The Initial Mass Function (IMF) gives the stellar mass distribution of a population as a function of the mass. Since some properties of a star depend on its initial mass, the IMF can control the ratio of cool and faint stars to hot and bright stars. The evolution rate of a star is also dependent on its mass, so the IMF also regulates the evolution of luminosity and colour of the population. Therefore, it is important to put constraints on the IMF in order to understand the spectrum of the galaxies. Some forms of the IMF generally used are ([6])-

1. Salpeter IMF -

$$\Phi(M)dM = \Phi_o M^{-2.35} dM \tag{1.12}$$

Here, m and dm are in units of solar mass $M_\odot$. Φ_o is a constant related to the local stellar density. The number of stars in a mass range decrease sharply with increasing mass in a Salpeter IMF. This IMF is generally used with a mass range of 0.1 $M_\odot$ - 100 $M_\odot$.

2. Kroupa IMF - In 2001, Pavel Kroupa derived a broken power law form of average IMF where

$$\Phi(M)dM = \begin{cases} \Phi_o M^{-0.3} dM & M < 0.08 M_\odot \\ \Phi_o M^{-1.3} dM & 0.08 M_\odot < M < 0.5 M_\odot \\ \Phi_o M^{-2.3} dM & M > 0.5 M_\odot \end{cases}$$

3. Gilles Chabrier determined an IMF (2003) for individual stars with M < 1

$$\Phi(M)dM = \begin{cases} \frac{0.158}{log(M)} e^{\frac{-(log(M)-log(0.0.08))^2}{0.952}} & M < 1 \\ \Phi_o M^{-2.3 \pm 0.3} dM & M > 1 \end{cases}$$

Stellar populations in the local universe can be used to count the stars as a function of mass and get a direct constraint on the IMF. The populations need to be very nearby for such counts to be accurate, as sub-solar dwarf stars, which make up majority of the mass in a stellar system, need to be counted for this constraint. Kinematics can also be used to determine the M/L ratio of star clusters or galaxies which can then be compared with luminosity to obtain the mass.

1.2.2 Probes of star formation rates

Star formation rates (SFR) can be probed using multi-wavelength probes and since massive stars dominate the light from stellar populations, most of these probes trace massive star formation rates. The continuum emission from stars also depends on their stellar mass and therefore these probes also trace different stellar mass ranges.

UV continuum emission

Although low mass stars dominate the total mass of a stellar population, at young ages, massive stars dominate the UV continuum emission. For a galaxy with Salpeter IMF and a constant star formation rate, the 1500 Åluminosity falls of by a factor of 100 after 10^8 years for solar metallicity. This luminosity also stabilises in the post main sequence phase of more massive and higher metallicity stars like the O type. This makes UV a good tracer for determining the SFR. The 1500 Åluminosity (ergs/s/Hz) is converted to the SFR ($M_\odot$/yr) as

$$SFR = \kappa_{1500} L_{1500} \tag{1.13}$$

UV emission suffers from dust attenuation from the dust grains in the interstellar and intergalactic medium. This can severely reduce the emission from galaxies and lead to an underestimate of the SFR. The UV light absorbed is re-radiated in infrared and a combination of both can be used to calculate the total SFR of a galaxy. Telescopes like ASTROSAT, HST and GALEX are used to observe in the UV band although at z $>$ 1.4, ground based optical observatories can also observed rest-frame UV emission.

Infrared emission

The 8-1000 μm integrated luminosity, L_{IR}, is a probe for the obscured SFR in galaxies. The UV emission is attenuated by the dust present in the ISM, IGM and the source galaxy itself. This absorbed light is re-emitted in infrared wavelengths. Old stellar populations also heat dust present in the ISM/IGM and contribute at the FIR wavelengths. Emission features from polycyclic aromatic hydrocarbons and absorption features from silicates can dominate the MIR emission from a galaxy depending on the ISM/IGM content. These features are mostly dominant at the MIR wavelengths and do not affect the FIR region of the spectrum. The integrated luminosity,L_{IR}, is used to determine the obscured SFR using the following relation -

$$SFR = \kappa_{IR} L_{IR} \tag{1.14}$$

Herschel Space Observatory has significantly improved the observations at FIR wavelengths and can observe galaxies close to the peak FIR emission. The peak emission along with observations at other wavelengths, is useful to prepare the dust emission model needed to calculate the total IR luminosity L_{IR}.

To get the total SFR and account for the dust attenuation, the results from UV (uncorrected for dust extinction) and IR can be added -

$$SFR_{Total} = \kappa_{UV} L_{UV} + \kappa_{IR} L_{IR} \tag{1.15}$$

Hα, O[II] and O[III]

Gas in HII regions can be excited and ionized from the UV emission from star formation in a galaxy and this can produce recombination lines like the Hα, which makes

them a direct tracer for SFR. Other emission line tracers like O[II] (3727 Å) and O[III] (5007 Å) are also used for tracing SFR but these features are subject to uncertainties resulting from excitation variation in galaxies and dust attenuation. Hα is regarded as the most reliable out of these emission line tracers. The calibration between the Hα luminosity and SFR is ([7]) -

$$SFR(M_{\odot}/yr) = 8.9 \text{ X } 10^{-42} L(H\alpha) E(H\alpha) \tag{1.16}$$

where L is the observed line luminosity in ergs/s and E is the extinction correction factor for Hα.

Radio emission

Radio emission from galaxies can be broadly from either synchrotron emission or thermal bremsstrahlung emission (also called free-free emission). The synchrotron emission is from the supernova accelerated electrons and has a steep spectrum with a power law index $\alpha = 0.8$ ([4]). Synchrotron radiation dominates the radio emission at frequencies ≤ 5 GHz. The thermal bremsstrahlung emission from electrons in HII regions contributes at higher frequencies and has a flat spectrum ($\alpha = 0.1$).

The supernovae responsible for accelerating the electrons in synchrotron emission can only be produced by stars with mass $> 8M_{\odot}$. These stars are also responsible for ionizing the HII regions. Since these accelerated electrons have a lifetime of $\leq 10^8$ years, radio emission is a tracer of recent star formation. The fact that radio emission is neither majorly affected by stars older than 10^8 years nor by dust extinction makes it a good tracer of SFR. Although there is still no direct relation between the radio emission and SFR, the well established Radio-FIR correlation (Yun et al 2001), which has been observed to hold upto z ≤ 4, can be used to calibrate the rest-frame 1.4 GHz luminosity to SFR. The Radio-FIR correlation has been observed to tightly hold for a span of many magnitudes in luminosity in the local galaxies. The Radio-SFR relation obtained this way is

$$SFR_{Radio}(M_{\odot}/yr) = (5.9 \pm 1.8) X 10^{-22} L_{1.4GHz}(WHz^{-1}) \tag{1.17}$$

This relation assumes a Salpeter IMF with mass limits 0.1 $M_{\odot}$ - 100 $M_{\odot}$ and the uncertainty in the relation comes mainly from the estimates of the local star formation density.

Radio emission is unaffected by dust extinction unlike the UV wavelengths. Radio interferometers have better arcsecond resolution and a wider field of view than present day FIR telescopes. These advantages make radio observations favorable. Strong radio emission can also come from non-star forming sources like AGNs and such sources can lead to an overestimate of SFR. Therefore it is necessary to removes such sources from the sample. From intermediate to high redshifts, radio continuum emission from galaxies is very difficult to detect individually. A stacking analysis for a large number of sources has been used in various studies (e.g. Panella et al. 2009) to statistically study these sources by pushing down the RMS noise levels way below that possible with present day radio telescopes. This comes at the cost that the individual properties of the galaxies can no longer be studied. But stacking analysis is a good method to understand the star formation properties of typical galaxy populations.

Chapter 2

2.1 Radio Interferometry

A radio interferometer, like the GMRT, measures the spatial coherence function of the electric field from the incoming electromagnetic radiation. This spatial coherence function, called the visibility, is then used to get the intensity as a function of co-ordinates on the sky. The visibility samples are obtained as a function of time and position on the u-v plane and are related to the intensity by a fourier transform. The spatial coherence function of the electric field can be written as -

$$V_\nu(\mathbf{r_1},\mathbf{r_2}) = \langle \iint_S E_\nu(\mathbf{R_1}) E^\star_\nu(\mathbf{R_2}) \frac{e^{2\pi\imath\nu|\mathbf{R_1}-\mathbf{r_1}|/c}}{|\mathbf{R_1}-\mathbf{r_1}|} \frac{e^{-2\pi\imath\nu|\mathbf{R_2}-\mathbf{r_2}/c|}}{|\mathbf{R_2}-\mathbf{r_2}|}\, dS_1\, dS_2 \rangle \tag{2.1}$$

where $\mathbf{R_1}$ & $\mathbf{R_2}$ are the position vectors of the points on the source on an imaginary celestial sphere of radius $|R|$, $\mathbf{r_1}$ & $\mathbf{r_2}$ are position vectors of the points of observation, $\mathrm{E}_\nu(\mathrm{R}_1)$ & $\mathrm{E}_\nu(\mathrm{R}_2)$ are the electric fields on the surface of the celestial sphere and dS_1 & dS_2 are elements of surface area on the celestial sphere. Under the assumptions that the radiation from source is not spatially coherent and the distance to the source is very large $|R|>>|r|$, this can be written as -

$$V_\nu(\mathbf{r_1},\mathbf{r_2}) = \int I_\nu(\mathbf{s}) e^{-2\pi\imath\nu\mathbf{s}.(\mathbf{r_1}-\mathbf{r_2})/c} d\Omega \tag{2.2}$$

where $\mathbf{s}$ is the direction vector $\mathbf{R}/|R|$, $I_\nu(\mathbf{s})$ is the intensity distribution of the radiation as a function of the direction $\mathbf{s}$ and $\mathrm{d}\Omega$ is the solid angle element. To simplify this expression, a coordinate system is chosen to measure the seperation variable in the coherence function in the units of wavelength such that $\mathbf{r_1}$ - $\mathbf{r_2}$ = λ(u,v,w). In

this coordinate system, direction vector s has the components (l,m,$\sqrt{1-l^2-m^2}$). Under the simplifying assumption that the radiation originates from a small part of the celestial sphere (l,m << 1), the visibility can be written as a two-dimensional Fourier transform -

$$V_\nu(u,v) = \iint I_\nu(l,m) e^{-2\pi\iota(ul+vm)}\, dl\, dm \tag{2.3}$$

A direct inversion of this Fourier transform will give the intensity distribution, which is

$$I_\nu(l,m) = \iint V_\nu(u,v) e^{2\pi\iota(ul+vm)}\, du\, dv \tag{2.4}$$

The spatial coherence function is sampled at various points on the u-v plane as the Earth rotates and this sampling is defined using a sampling function S(u,v) which is zero for points without a measurement. This gives an intensity distribution I^{D}_{ν}(l,m) called the dirty image and can be expressed as -

$$I^{\mathrm{D}}_\nu(l,m) = \iint S(u,v) V_\nu(u,v) e^{2\pi\iota(ul+vm)}\, du\, dv \tag{2.5}$$

The dirty image is related to the true image (the true intensity distribution) by a convolution, i.e. $I^{D}_{\nu}(l,m) = I_\nu(l,m) \star P(l,m)$. Here, P(l,m) is the point spread function or the synthesised beam, which is a Fourier transform of the sampling function.

2.2 Self-Calibration

Calibration is a crucial step to obtain the true intensity distribution of the sky from observed visibilities. Errors in the amplitudes and phases of the visibilities can create artifacts on the image like negatives and ripples near sources. The observed and true visibilities are related as -

$$V^{\mathrm{obs}}_{\mathrm{i,j}}(t) = g_i(t) g_j(t) G_{i,j}(t) V^{\mathrm{true}}_{\mathrm{i,j}}(t) + \beta_{i,j}(t) + \gamma_{i,j}(t) \tag{2.6}$$

where $g_i(t)$ and $g_j(t)$ are complex gain factors of individual antennas, $G_{i,j}(t)$ is the baseline based complex gain factor, $\beta_{i,j}(t)$ is the term representing thermal noise and $\gamma_{i,j}(t)$ is an additive offset term. The effects of $G_{i,j}(t)$ and $\gamma_{i,j}(t)$ can be reduced by

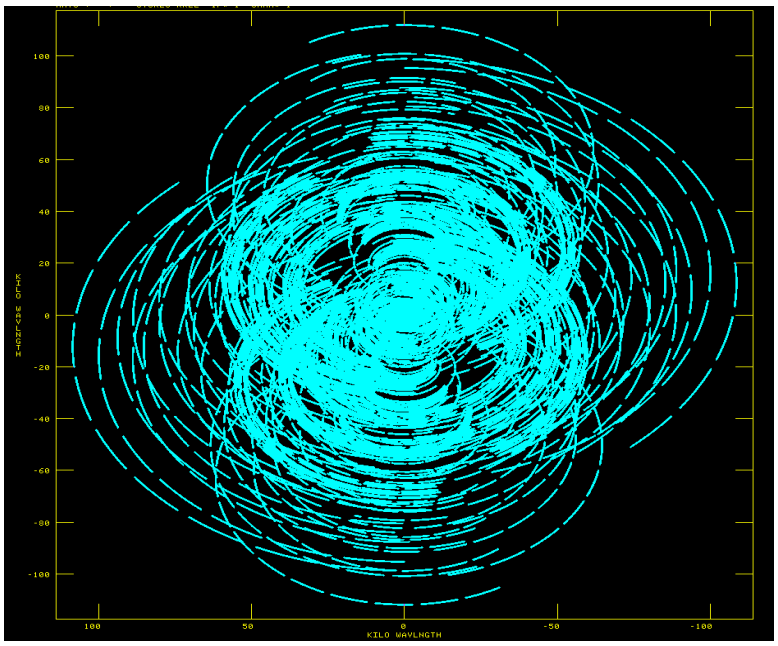

Figure 2.1: U-V coverage of a single channel from an 8 hour dataset with the GMRT for this study ($\delta = 52^o54'$)

good design and can therefore be ignored. Ordinary calibration relies on a calibrator source of accurately known flux density, structure and position in the sky for obtaining the gain factors. This calibrator source may be in a different part of sky which might give inaccurate values of the gain factors due to atmospheric observations. This error also depends on the frequency of the observations of the calibrator, which can be problematic if it is not close to the source position as there a very limited number of such calibrator sources in the sky.

The basic idea behind self-calibration is to let the gain factors be free parameters and then solve for them [8]. The aim is to make an astronomically plausible model I_{mod} which when Fourier transformed to V_{mod} and multiplied by the gain factors, gives the observed vibility within the noise levels. Minimizing the sum of squares of residuals by adjusting $g_i(t)$ and $g_j(t)$ is one method for self-calibration. The sum of squares of residuals can be written as

$$V^{\rm obs}_{\rm i,j}(t) = g_i(t)g_j(t)G_{i,j}(t)V^{\rm true}_{\rm i,j}(t) + \beta_{i,j}(t) + \gamma_{i,j}(t) \tag{2.7}$$

The errors in the model are averaged down depending on the number of array elements. The iterative algorithm for self-calibration then is -

1. The first source model is made using any constraints available on the source structure.

2. Divide the source by the model visibility to convert it to a point source.

3. Solve for the complex gain factors.

4. Calculate the corrected visibility using the obtained complex gain factors - $V^{\rm corr}_{\rm i,j}(t) = V^{\rm obs}_{\rm i,j}(t)/g_i(t)\ g^{\star}_{\rm j}(t)$.

5. Make a new model using the corrected visibility and the constraints on source structure and then repeat from step 2.

This iterative procedure of self-calibration is most successful for a large number of antennas and good u-v coverage. The requirement for this method is that the total number of degrees of freedom must be greater than the number of independent visibilities. Self-calibration might fail if the source structure is complex or the signal-to-noise ratio is too small.

2.3 Extended Groth Strip

The Extended Groth Strip (EGS, $\alpha = 14h17min, \delta = 52^{\circ}$ 30') is a deep field near the constellation of Ursa Major. This field has been deeply imaged and extensively studied in multiple wavelengths from X-ray to radio like in the All-Wavelength Extended Groth Strip International Survey ([10]). There were multiple reasons for choosing this field for the study. The EGS has a larger area than other deep fields like the combined GOODS fields[11] and a similar wavelength coverage range. This makes it possible to look for exotic objects which might not be possible in smaller fields. Their is a wide variety of deep multi-wavelength data available from X-ray to Radio obtained using Chandra, GALEX, Hubble, Keck, Subaru, Palomar, Spitzer, VLA, MMT and CFHT telescope from different studies. ([10]). It is one of the darkest and most dust-free regions of the sky and also has low Galactic and zodiacal infrared emission which makes it a good field for deep imaging with long observations.

At the moment, there is still no deep radio (1.4 GHz) continuum image availabe of the EGS. The VLA image available has an RMS noise of only $\sim$ 20 μJy/Beam ([2]), far poorer than that of the other extra-galactic deep fields. Stacking analysis of sources in this field requires accurately determined redshifts which are available from the DEEP2 survey ([12]). The GMRT observations used for this study covered

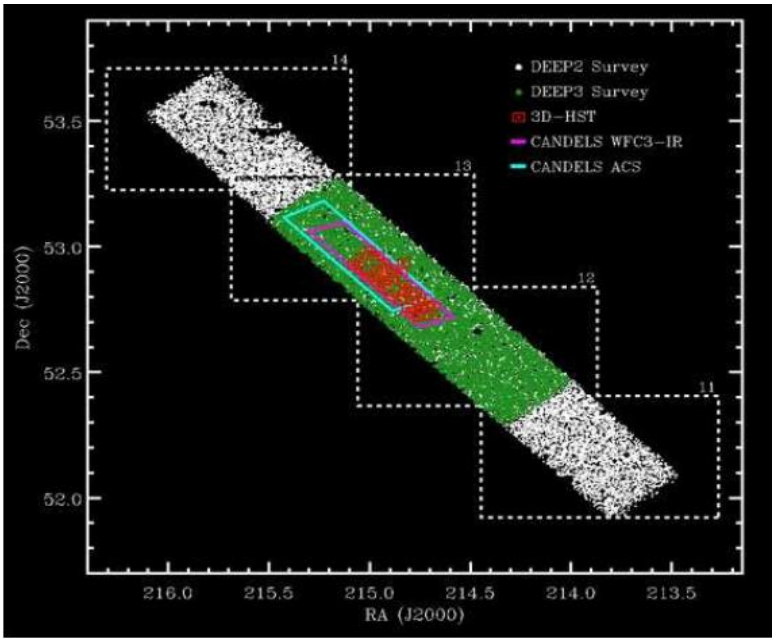

Figure 2.2: The Extended Groth Strip as covered by DEEP2 and DEEP3 surveys.

the central 0.5 degree X 0.5 degree of the EGS which overlaps with the DEEP2 and DEEP3 coverage and also covers the CANDELS and 3D-HST regions (Figure).

The DEEP2 survey is the largest high-precision redshift survey of galaxies at z $\sim$ 1 till date, done using the high spectral resolution modes of the DEIMOS spectrograph at the Keck telescope ([12]). DEEP2 is a magnitude limited (limiting apparent magnitude of $R_{AB} = 24.1$) survey of galaxy redshifts in four seperate fields. The total number of objects obtained with secure redshifts is 38,348. The survey covers an area of 2.8 deg^2 which is divided into four fields, first of which was the EGS.

2.4 GMRT Data

For this study, 57 hours of on source EGS data from the GMRT was used. The GMRT data was calibrated using '1400+621' as the phase calibrator and 3C147, 3C286 and 3C48 as the flux calibrators, which are quasars. AIPS was used for flux, phase and bandpass calibration of the visibility data. All individual datasets were first imaged in AIPS and then combined with the appropriate calibration table applied to it. The combined dataset was then self-calibrated using a high quality image from one dataset to get the final image from AIPS. This image had an RMS of 7.5 μJy. AIPS uses faceting method for imaging. The field is divided into several facets and the 2-D

approximation such that the 2-D approximation (Eq 1.4) is valid for each facet. Information about the data is given in the table below

Visibility Data information	
Parameter	Value
Central Frequency	1381.2 MHz
Bandwidth	33.33 MHz
Channels	512
Pixel Size	0.4 arcseconds
Number of Facets	40
Primary Beam FWHM	21.3 arcminutes
Synthesized Beam FWHM (R.A. x Dec)	1.9 x 1.8 arcseconds
Phase center position	RA - 14h 19m 59.99s Dec - $52^o54'$
On Source Time	57 hrs

CLEAN in CASA was used to image the combined calibrated dataset because it uses the W-projection algorithm ([13]), which is used to make a single image instead of facets. The RMS for the image was 8.8 μJy with a resolution of 1.9 x 1.8 arcseconds. A primary beam correction was then done to the image in AIPS using PBCOR. An eighth order polynomial is fit to the GMRT primary beam of the form ([14]) -

$$1 + \frac{ax^2}{10^3} + \frac{bx^4}{10^7} + \frac{cx^6}{10^{10}} + \frac{dx^8}{10^{13}} \tag{2.8}$$

At an observing frequency of 1280 MHz, a = 2.27961, b = 21.4611, c = = 9.7929 and d = 1.80153. A zoomed in part of the image after primary beam correction in AIPS is shown below.

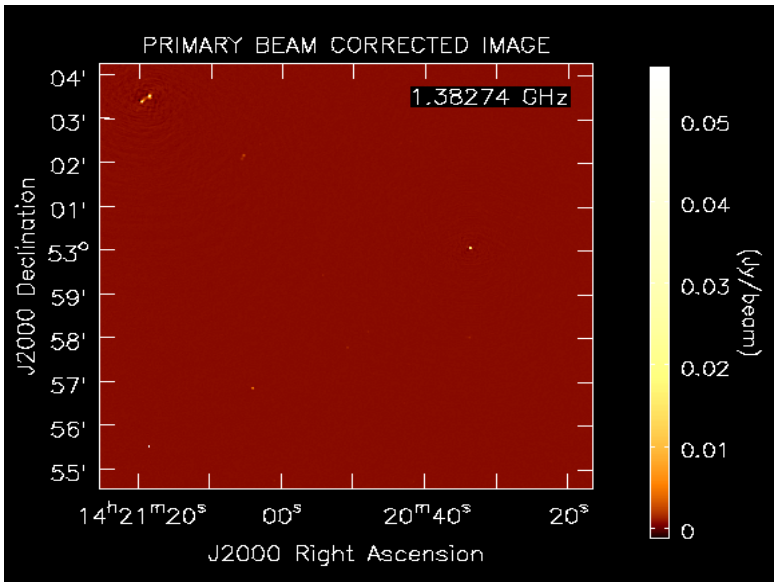

Figure 2.3: Primary beam corrected image of the EGS (zoomed in)

Chapter 3

3.1 Selection Criteria for Stacking

The DEEP2 catalogue ([12]) was used to identify the position of the sources in the final image for the stacking analysis. DEEP2 catalogue provides reliable redshift measurements of $\geq$38000 galaxies along with their sky positions, rest frame B-band magnitude M_B and U - B colour. The M_B and U - B colour data can be used to estimate the stellar mass and unobscured star formation rate of the galaxies in the DEEP2 sample. The stellar masses and the optical star formation rates of the DEEP2 galaxies were estimated using calibrations from Weiner et al. (2009, [15]) and Mostek et al. (2012, [16]). The SFR calibration by Mostek et al. (2012) assumes a Salpeter IMF but the stellar mass calibration assumes a diet Salpeter IMF.

The codes for applying the selection criteria and stacking the sources were written in Python by Apurba Bera (Bera et al, 2017, in prep) at NCRA-TIFR, Pune for a project. They were provided with the stellar mass and optical SFR estimates by Benjamin J. Weiner, after converting the optical SFR estimates to a Chabrier IMF by subtracting 0.15 dex. They then converted both the stellar mass and optical SFR estimates to a Salpeter IMF by adding 0.15 dex to the values provided by Benjamin J. Weiner, to keep it consistent with the SFR-radio calibration used.

After the primary beam correction, the RMS of the image increases with distance from the center. After the half power points, the RMS is more than twice of that at the center. To reduce the RMS in the final stacked images, all sources beyond the FWHM were rejected. Within the FWHM, 2151 sources were identified using the DEEP2 catalogue although most of them are not detected individually from the final continuum image. To reduce the RMS and effect of biases from the sample of galaxies, the below mentioned selection criteria were applied -

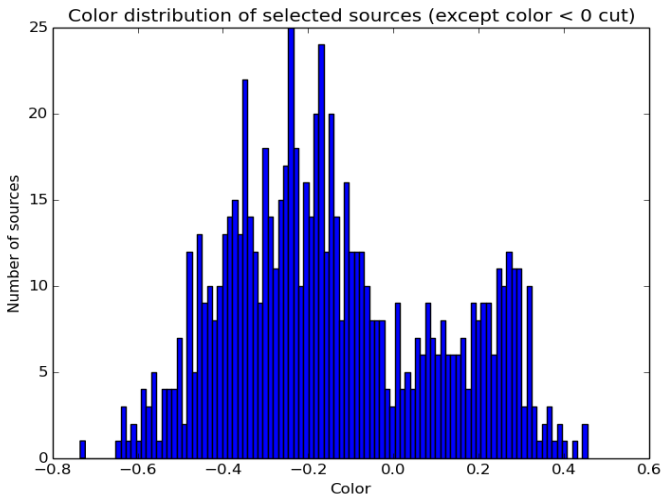

Figure 3.1: Colour histogram of selected sources (except Colour < 0) shows a bi-modality about colour $= 0$

1. Active Galactic Nuclei (AGN) are strong non-star forming sources of radio emission. It is usually assumed that in the local universe, 1.4 GHz luminosities greater than 2 10^{23} W/Hz are mostly produced by AGNs. Since these AGNs could contaminate the sample and over-estimate the SFR, they have to be removed from the sample. Sources with any pixel brighter than 10σ (where σ is the local RMS of the 50 x 50 pixel box), within a radius of 2.8" from its reference position (DEEP2 catalogue), were rejected. This was done to remove such likely AGNs from the sample.

2. In order to have only typical star forming "blue" galaxies, colour was calculated using the definition ([17])

$$Colour = (U - B) - (0.0032(M_B + 21.62)) + 1.035 \tag{3.1}$$

   Colour distribution of galaxies shows a clear bi-modality about colour $= 0$ (Figure 2.1). The "red" galaxies (galaxies with colour > 0) are systems with little or no star formation and are not the focus of this study. The "blue" galaxies (Colour < 0) are the typical active star forming galaxies since young stars mostly emit UV radiation and correspond to the bluer end of the spectral class of stars. The focus of this study is on typical star forming galaxies and therefore for the final sample, galaxies with colour < 0 were selected.

3. Faint sources at high-redshift are less likely to be detected than that at lower redshifts. This makes the sample biased towards brighter sources at high redshifts. A magnitude cut was applied to the identified sources to remove this bias. The DEEP2 survey covers an area of 2.8 deg^2 divided into four separate fields observed to a limiting apparent magnitude of R_{AB} = 24.1. This corresponds to an absolute blue magnitude of M_B = -20 at z $\sim$ 1. The redshift range of the sample for the study is z = 0.2-1.45. For this study, galaxies with M_B<-20 were selected in order to remove the bias towards brighter galaxies to some extent. This does not make the sample complete throughout the redshift range as R_{AB} = 24.1 corresponds to M_B = -21.1 at z $\sim$ 1.4 but with that criteria there are too few sources in the final sample, so M_B<-20 was used to select sources for the final sample for the study.

4. For each source identified using the DEEP2 catalogue, the RMS was calculated within a box of 50 pixels x 50 pixels (20" x 20") centered at the position of the source. A histogram of the RMS of all boxes was plotted to check the distribution (Figure 2.2). A "10% tail" was defined as the part of the distribution starting from the point beyond which the number of galaxies per bin falls below 10% of the maximum frequency bin in the distribution. Galaxies lying within this 10% tail were rejected so as to reduce the RMS in the final stacked images without loosing a large number of sources from the sample. The 10% tail part of the distribution for this sample lies beyond 20 μJy.

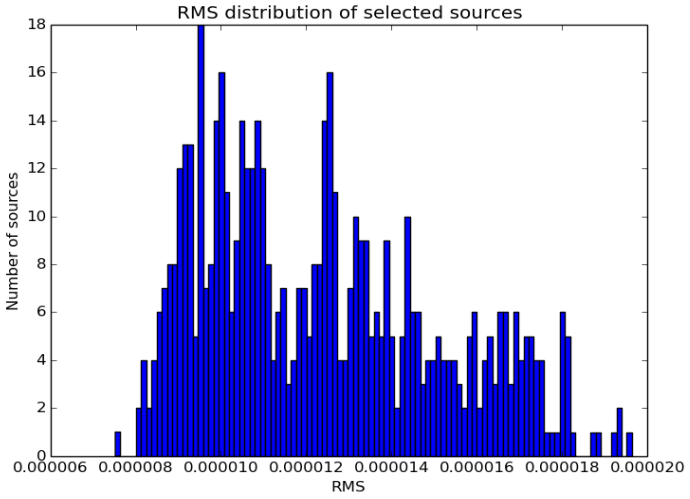

Figure 3.2: RMS distribution of selected sources with sources beyond 20 μJy removed from the sample

After applying all the selection criteria, a total of 570 sources were left in the final sample which was used for this study. Distributions of redshift, stellar mass, optical SFR and colour are shown in Figure 2.3 below. The median value of each distribution is also mentioned. The redshift range for the sample is z = 0.23-1.44. Number of galaxies show a slight decrease with redshift in the distribution because of the magnitude limit of the survey, which is likely to cause a bias towards brighter galaxies at high redshifts in the sample. The stellar mass range of the galaxies in the sample is $10^{9.4}$ $M_{\odot}$ to $10^{11.5}$ $M_{\odot}$ with the distribution peaking at $\sim 10^{10.3}$ $M_{\odot}$. The optical SFR range of the sample is from $10^{0.36}$ $M_{\odot}$/yr to $10^{2.02}$ $M_{\odot}$/yr with the peak at $10^{0.85}$ $M_{\odot}$/yr. Colour distribution is also shown in Figure 2.3 where the range is -0.735 to -0.0009 (after selecting for blue galaxies) with the peak at -0.173.

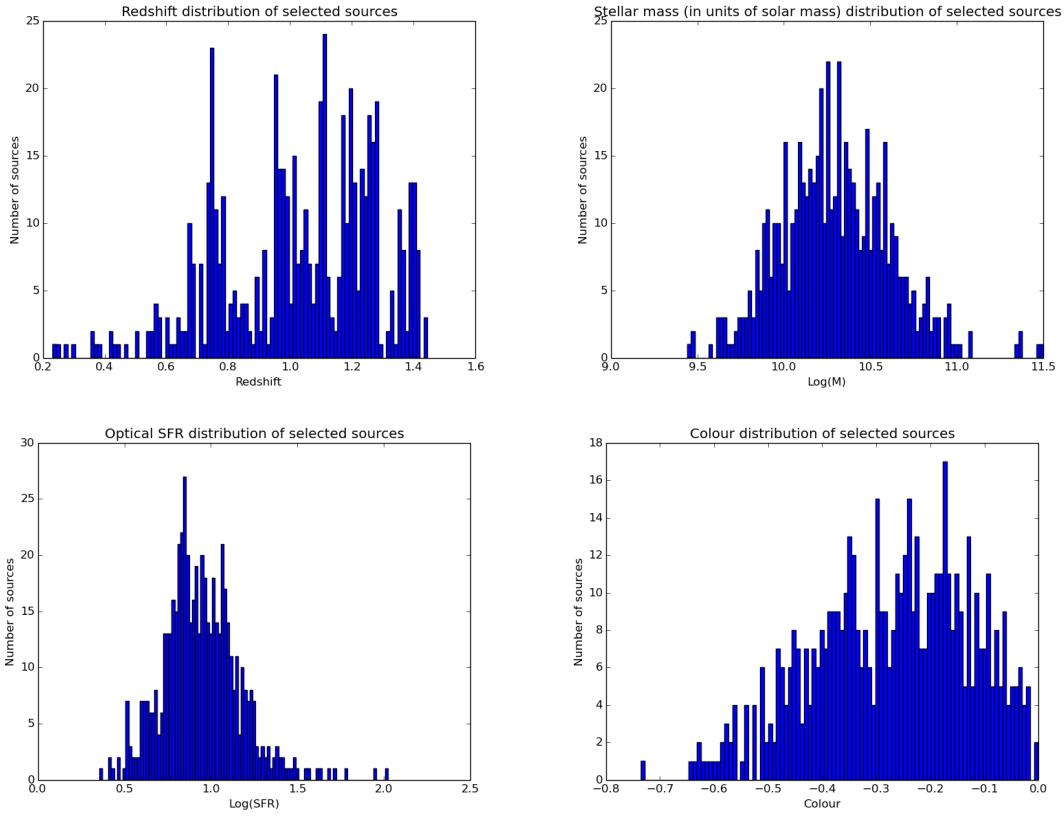

Figure 3.3: (top-left) distribution of the selected galaxies with median z = 1.06. (top-right) Stellar mass distribution of selected galaxies with median = $10^{10.28}$ $M_{\odot}$. (bottom-left) Optical SFR distribution of selected galaxies with median optical SFR = $10^{9.3}$ $M_{\odot}$/yr. (bottom-right) Colour distribution of selected sources with median colour = -0.257

3.2 Radio Stacking

Radio continuum emission at low frequencies from typical star forming galaxies is very faint at z > 0.1, which makes them almost impossible to detect with present day radio telescopes. A stacking analysis allows us to study these individually undetected galaxies by reducing the noise around them to levels lower than that possible with present day radio telescopes. Stacking is a statistical method of studying a population of galaxies and cannot reveal information about individual galaxies. This is not a big price to pay if we are looking to study the properties of a typical population.

For this study, the median stacking method (White et al., 2007,[18]) was adopted as it has several advantages over the mean. AGN contamination is a serious problem in such samples as most present day surveys are likely to include them. It is extremely important to avoid such strong non-star forming sources of radio emission from the sample. The median stacking method is more robust to the outliers in the population than the mean and the noise still goes down as $1/\sqrt{N}$. This prevents overestimation of star formation rates which is why the median is a good representative of the typical population which in this case is the population of typical star-forming galaxies.

Sources that satisfied the selection criteria were identified using optical positions from the DEEP2 catalogue first and then a 50 x 50 pixel box was cut around that position. This size of region was chosen so that the local RMS could be calculated for a sufficient number of independent pixels. Then using the median stacking method, a median of each corresponding pixel from the sample of cut-outs was taken to make the stacked image. The median stacked image was then analysed using the task JMFIT in AIPS to see whether there was a detection or not. Figure 2.4 shows the stacked images. The images were stacked in flux density. Image on the left showed a clear detection of 13.5σ where the peak flux density was 8.34 μJy and the integrated flux density was 9.93$\pm$1.21 μJy. The RMS in the image was 0.58 μJy. To test for systematic effects, stacking was also done with a 50 pixel offset (Figure 2.4) in RA to check if there is any detection and there was no evidence of detection in such image. The RMS in the offset stacked image was 0.49 μJy, which is lower than the stacked image with detection, which could be because of the presence of sources in the cut outs used for that image. The theoretical noise for stacked image was $9/\sqrt{570}$ μJy = 0.38 μJy.

The stacking of the selected sources was done in luminosity, i.e. the fluxes were first converted to 1.4 GHz luminosity and then median stacked. To obtain the 1.4GHz rest-frame luminosity, the redshifts from DEEP2 catalogue were first used to calculate the

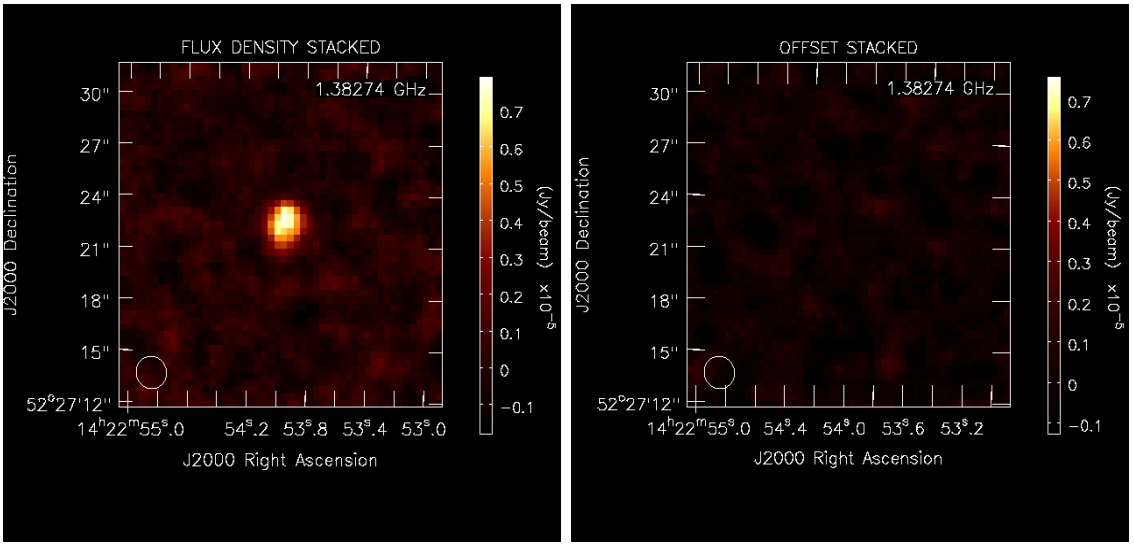

Figure 3.4: (left)Flux density stacked image with a 13.5σ detection. RMS = 0.58 μJy. (right) Flux density stacked image with offsets in source position show no evidence of detecion. RMS = 0.49 μJy.

rest frequency of emission.The luminosity distance and a spectral index of 0.8 ([4]) were then used to find the rest frame 1.4 GHz luminosity. For specific SFR, each galaxy was first divided by its stellar mass and then stacked in luminosity per unit mass. The rest frame 1.4 GHz luminosity was converted to SFR using the relation ([1])-

$$SFR(M_{\odot}/yr) = (5.9 \pm 1.8)x10^{-22}L_{1.4GHz}(WHz^{-1}) \tag{3.2}$$

which assumes a Salpeter IMF with mass limit 0.1-100 $M_{\odot}$ and uses the radio-FIR correlation. The uncertainity in the relation comes mainly from the estimates of the local star formation density. The median total SFR obtained from stacking all 570 sources in the sample was 20.19$\pm$1.24 $M_{\odot}$/yr ($\pm$6.16 $M_{\odot}$/yr) for a median redshift 1.061. The sources were divided in bins of redshift, stellar mass and colour to study their behaviour with these parameters. Median stacking was then done in each bin such that a detection with sufficiently high significance was obtained (>5σ atleast). The number of bins were chosen such that each bin has enough sources for a detection. The stacked emission appeared to be resolved for some bins with lower number of galaxies. In the case of bins with large number of galaxies, most of the sources lie very close to the centre and make the stacked emission unresolved. In case of resolved emission, the integrated flux was used as the total flux whereas the peak flux was used to represent the total flux in case of unresolved emission. For this project, the values

of the cosmological paramters used are $H_o = 68\ kms^{-1}\ Mpc^{-1}$, $\Omega_m = 0.32$ and a flat universe was used for the analysis.

Chapter 4

4.1 Evolution with redshift

The evolution of total median SFR and specific SFR with redshift was studied by making bins in redshift and then stacking the luminosities in each bin. In SFR vs redshift study, all detections were $>5\sigma$. Images obtained after stacking in each bin were analysed using the task JMFIT in AIPS, where a Gaussian fit was applied to the stacked emission. The peak or integrated values from the fit were used depending on whether the emission in the stacked image was resolved or unresolved. I would like to state that there are effects of sample variance in the analysis and they have not been accounted for in this project.

The total median SFR was found to be increasing in the redshift range 0.2-0.8 which has been found in previous works like Noeske et al. (2007) [19], Bera et al. (2017,in prep) etc. Figure 3.1 shows the plot between median total SFR and redshift for this study along with the Bera et al. and optical SFRs. Bera et al. did a study on three DEEP2 fields using deep continuum images from 610 MHz GMRT data and a stacking analysis. The optical SFRs for DEEP2 galaxies were obtained by Benjamin Weiner ([15]) using M_B and U - B colour and the values used here are for the same subset of galaxies. A power law of the form SFR = $\mathrm{A}(1+z)^n$ was fit to the data only upto z = 0.8 because cosmic star formation density is found to increase as a power law upto z$\sim$1 ([20]) and flatten out after that before eventually decreasing. The fit parameters were A = 0.51$\pm$0.19 and n = 6.95$\pm$0.79 for the power law function. The sample has a bias towards brighter galaxies at high redshifts due to the magnitude limit in which case the total SFR could be overestimated for high redshift bins. The data points here are all $>6\sigma$ significance.

The specific star formation rate (sSFR) of a galaxy is defined as the ratio of the total SFR to the total stellar mass of the galaxy. The sSFR gives an idea about the

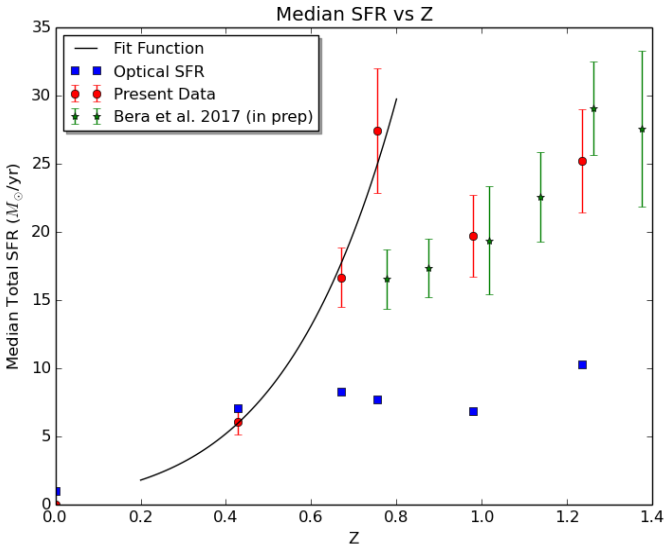

Figure 4.1: SFR vs redshift for the sample. Power law is fit only upto z = 0.8.

star formation history of the galaxy, whether it is in an active or passive phase of star formation. A high sSFR means that the galaxy is actively star forming and that a large fraction of the stars in it are young. The sSFR for the sample was also found to be increasing with redshift. The optical specific SFR was calculated using the optical SFRs and stellar masses of the galaxies from the DEEP2 catalogue. The specific SFR (in Gyr^{-1} was found to be increasing (Figure 3.2) with redshift as

$$sSFR = A(1+z)^n \tag{4.1}$$

The fit parameter values obtained were A = 0.09±0.03 and n = 3.29±0.49. Bera et al. found the value of A = 0.074±0.017 and n = 3.67±0.31 for z = 0.7 - 1.4 with the DEEP2 fields. The increasing trend was also found previously for massive galaxies at redshifts of z = 0 - 1.8 with n = 5.0±0.4 by Damen et al.(2009,[21]) and for LBG galaxies at z ∼ 2 - 5 with n = 1.0±0.1 by Gonzalez et al. (2014,[22]). The value of the exponent in the power law, n, seems to be decreasing with redshift from these studies.

The dust attenuation factor was calculated using the ratio of total median SFR to optical SFR and plotted with redshift (Figure 3.2). Bera et al. found no significant evolution of dust attenuation factor with redshift in their study, but the factor seems to increase with redshift from our study.

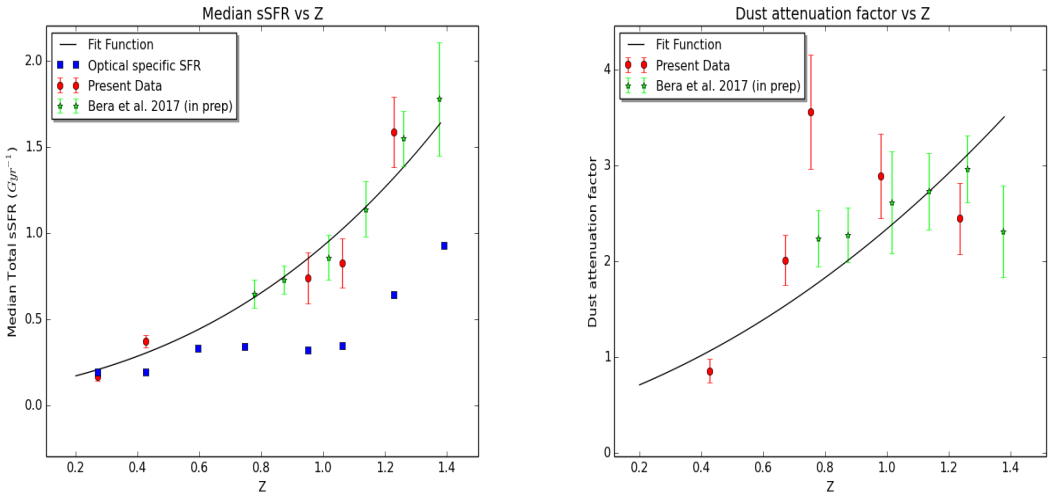

Figure 4.2: (left)Specific SFR (Gyr^{-1}) vs redshift for the sample. (right) Dust attenuation factor vs redshift for the sample.

4.2 Behaviour with Colour

The total SFR showed a strong dependence on colour, increasing with increasing colour of the galaxies, where the colour was calculated using Eq 2.1. The plot (Figure 3.3) shows that total SFR is higher for "redder" blue galaxies.

The specific SFR showed a decreasing trend with colour (Figure3.4), which shows that the stellar mass of galaxies increases more steeply with colour than total SFR and implies that bluer galaxies are forming a relatively higher fraction of their stellar mass han "redder" blue galaxies. A function of the form sSFR = 10^{bx+a} was fit to the data and the fit parameters obtained were a = -0.41±0.16 and b = -1.51±0.48. The dust attenuation factor increased with increasing colour which shows that galaxies with higher dust content have higher star formation rates as the dust content promotes formation of stars and attenuates the UV and optical emission from these galaxies. The fit parameters for a similar function fit to these points were a = 0.83±0.22 and b = -1.59±0.96

4.3 SFR and Stellar Mass

In star forming galaxies, the star formation rate and stellar mass have been found to be tightly correlated by several studies ([23],[24]). This correlation of star forming

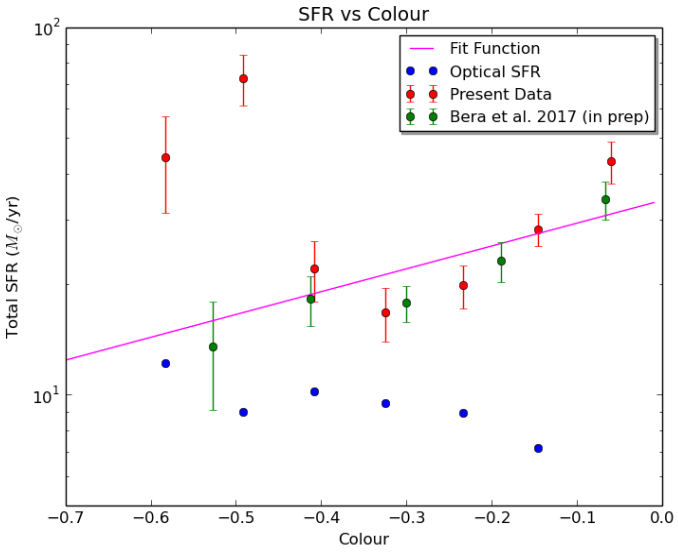

Figure 4.3: SFR vs colour for the sample. Power law of the form SFR = 10^{bx+a} was fit to the data.

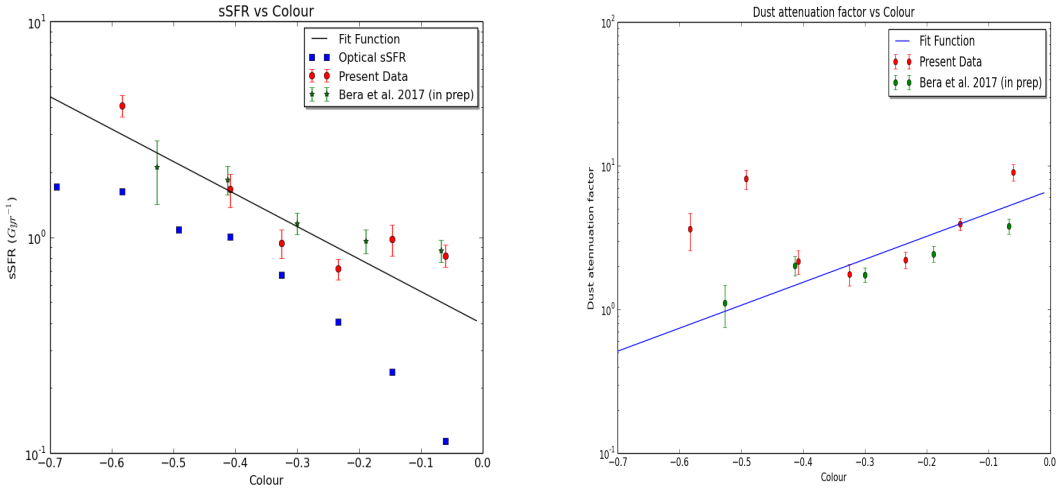

Figure 4.4: (left)Specific SFR (Gyr^{-1}) vs colour for the sample. (right) Dust attenuation factor vs colour for the sample with the fit function 10^{bx+a}.

galaxies is known as the "Main Sequence" (Noeske et al., 2007) where log(SFR) is approximately proportional to log($M_\star$). Noeske et al. (2007,[19]) did a multi-wavelength analysis of the EGS and estimated the width of the main sequence to be $\sim$0.3 dex which does not seem to vary upto z $\sim$ 1.1. The main sequence can be expressed as -

$$log(SFR) = n(log(M_\star)) + a \tag{4.2}$$

where n is the slope and a is the intercept. It can also be written as -

$$SFR = A(\frac{M_\star}{10^{10} M_\odot})^n \tag{4.3}$$

where A is the normalization. Noeske et al. (2007) studied a stellar mass range of 10^{10} $M_\odot$-10^{11} $M_\odot$ and the redshift range of 0.2 - 0.7. They found the slope to be significantly less than unity and to flatten out at higher redshifts. They also found that the whole main-sequence appears to shift upwards with redshift. Elbaz et al. (2007,[25]), based on their studies on GOODS and SDSS galaxies at redshifts of z $\sim$ 1 and z $\sim$ 0 respectively, found that the slope appears to be slightly larger at higher redshifts.s found that the slope appears to be slightly larger at higher redshifts. Bera et al. obtained a slope value that matches well with that of Panella et al (2009,[26]) and Elbaz et al. (2007,[25]) where the former was obtained using radio observations of BzK galaxies at high redshifts. Figure 3.5 shows the plot for SFR and stellar mass of galaxies.

The value of n obtained for this sample was 0.9$\pm$0.1 and A = 9.53$\pm$1.65. The slope obtained in this study is in agreement with that obtained by Elbaz et al. (2007,[25]) with their study on GOODS field. It is also within 1σ agreement with that obtained by Bera et al.. The slope of the main sequence obtained here is within 2σ agreement of that obtained by Noeske et al.(2007,[19]), 0.5 σ agreement with Pannella et al. (2009,[26]) and within 1σ agreement with Pannella et al. (2015,[27]) who did a multi-wavelength study on GOODS-N field. Due to the bias towards brighter galaxies at high redshifts, introduced by the magnitude limit of the sample, the normalization can appear larger than the actual value although the slope is not affected. A table below lists compares results from this study and other such studies -

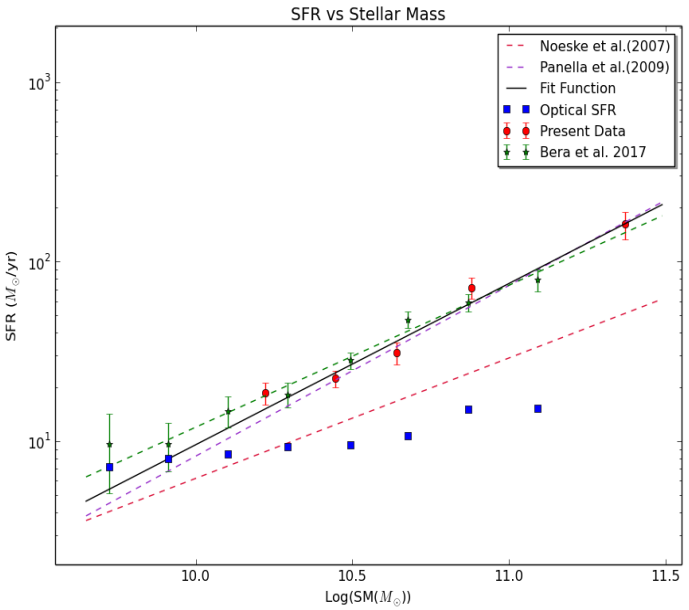

Figure 4.5: SFR vs Stellar Mass for the sample shows tight correlation between the two.

Main sequence studied by various works				
Study	Field/Galaxies	$M_\star$ range	Z range	n (slope)
Present Study	EGS	$10^{9.4}M_\odot$-$10^{11.5}M_\odot$	0.2-1.45	0.9±0.1
Bera et al. (2017)	EGS	$10^{8}M_\odot$-$10^{12}M_\odot$	0.7-1.4	0.79±0.05
Noeske et al. (2007)	EGS	$10^{10}M_\odot$-$10^{11}M_\odot$	0.2-0.7	0.67±0.08
Elbaz et al. (2007)	GODDS	$10^{9}M_\odot$-$10^{11}M_\odot$	0.8-1.2	0.9
Pannella et al. (2009)	COSMOS,BzK	$10^{10}M_\odot$-$10^{11}M_\odot$	∼2	0.95±0.07
Pannella et al. (2015)	GOODS-N	$10^{9}M_\odot$-$10^{11}M_\odot$	0-1.5	0.8±0.08

The specific star formation was found to be decreasing with the increasing stellar mass (Figure 3.6) as -

$$sSFR = n(log(M_\star)) + a \tag{4.4}$$

The slope (n) obtained from this study was n = -0.19±0.05 and a = 1.09±0.07. In similar studies, Elbaz et al. (2007, [25]) estimated a slope of n = -0.1 for galaxies in GOODS at z = 0.8 - 1.2. This value varies between different studies, which could be a result of various biases. The decreasing trend indicates that lower mass galaxies are forming a larger fraction of their stellar mass today compared to what they were

forming in the past. One possible explanation for this could be the "cosmic downsizing", i.e. the shift from more massive to less massive galaxies in the galaxy population dominanting star formation.

The sSFRs of this study can be overestimated because of the bias in the sample towards high SFR galaxies. The dust attenuation factor has been found to be strongly dependent on the mass of the galaxy in previous studies (Pannella et al., 2009, 2015; Oteo et al., 2014 [28]). The dust attenuation factor (DAF) estimated here also turns out to be strongly dependent on mass. The function fit to the plot is -

$$log(DAF) = b\text{x}log(M_\star) + a \tag{4.5}$$

The best fit values obtained were b = 0.74±0.22 and a = -7.26±2.37. Bera et al also found a similar increasing trend of DAF with stellar mass. This is in line with the general assumption that more massive galaxies have higher dust content leading to more dust attenuation.

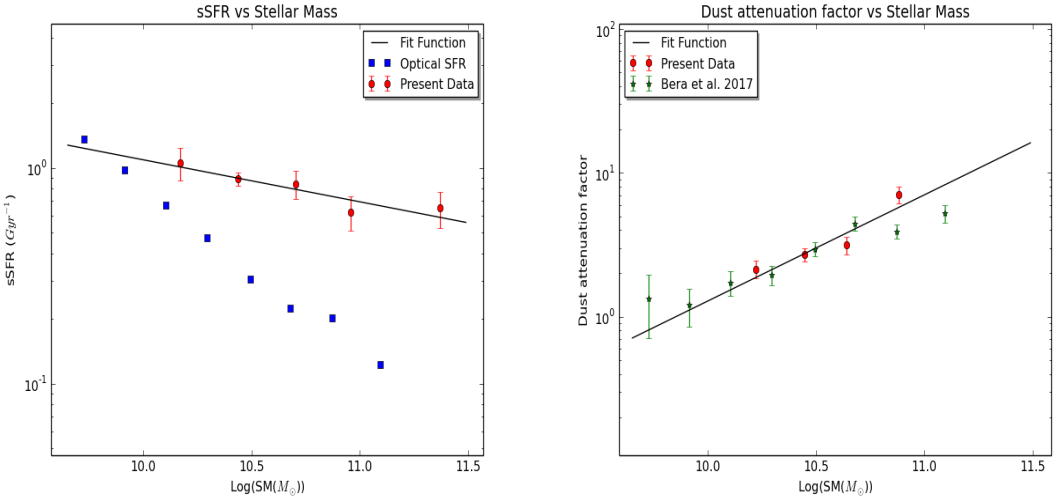

Figure 4.6: (left)Specific SFR (Gyr^{-1}) vs stellar mass for the sample. (right) Dust attenuation factor vs stellar mass

To check the evolution of the main sequence with redshift, binning was done in stellar mass for redshift ranges of 0.2-1.0 and 1.0-1.45. In their multi-wavelength study of the EGS, Noeske et al. 2007 ([19]) found that the slope of main sequence seems to flatten towards high redshifts for $M_\star$ in the range $10^{10}M_\odot$-$10^{11}M_\odot$ for z = 0.2-0.7 and that the main sequence appears to shift upwards with increasing redshift. Elbaz et al.2007 ([25]) found the slope to be slightly larger at higher redshifts based on their

studies of GOODS (at z $\sim$ 1) and SDSS (at z $\sim$ 0) galaxies. Panella et al. 2015 ([27]) did a multi-wavelength study on the GOODS-N field and found the normalization of the main sequence to be increasing with redshift. Figure 3.7 shows the main-sequence plot for the two redshift ranges in this study.

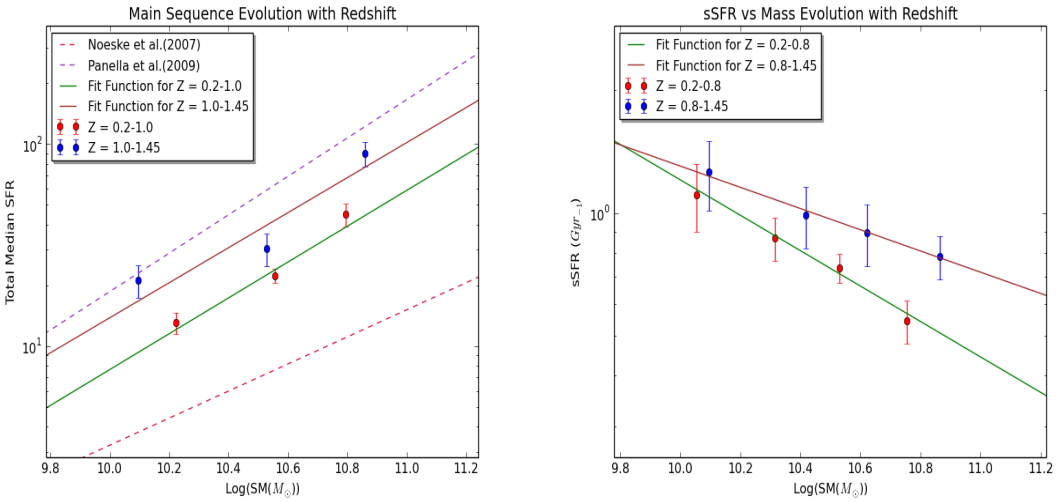

Figure 4.7: (left) Main sequence plots for Z = 0.2-1.0 and Z = 1.0-1.45. (right) sSFR (Gyr^{-1}) vs Stellar Mass for Z = 0.2-0.8 and Z = 0.8-1.45.

The intercept in Figure 3.7 was a = -7.98$\pm$2.31 for Z = 0.2-1.0 and a = -7.52$\pm$3.79 for Z = 1.0-1.45. The slopes of the main sequence were n = 0.89$\pm$0.21 for Z = 0.2-1.0 and n = 0.87$\pm$0.36 for Z = 1.0-1.45. There seems to be no significant change in the intercept or the slope of the main sequence with redshift from these plots, which could be because of a very small number of datapoints.

The specific SFR vs stellar mass relation was also studied for two redshift ranges; Z = 0.2-0.8 and Z = 0.8-1.45 (Figure 3.7). The slope was found to be less steeper for the higher redshift range, which implies that relatively, more massive galaxies are forming stars less actively today than in the past and vice versa for lesser massive galaxies. A power law of the form log(sSFR) = n(log(SM)) + a, was fit to the data and the fit parameters were - For Z = 0.2-0.8 : n = -0.43$\pm$0.04, a = 4.41$\pm$0.49 and for Z = 0.8-1.45 : n = -0.26$\pm$0.01, a = 2.71$\pm$0.18.

Bibliography

[1] Yun M. S. et al., 2001, ApJ, 554, 803

[2] R. Ivison et al. 2007, ApJ, 660, L77

[3] Jeffrey A. Newman et al., The DEEP2 Galaxy Redshift Survey: Design, Observations, Data Reduction, and Redshifts, ApJS, 2013.

[4] Condon J. J., 1992, ARAA, 30, 575

[5] Low Frequency Radio Astronomy, NCRA-TIFR, Pune. Editors - Jayaram Chengalur, Yashwant Gupta and K.S. Dwarkanath.

[6] Cosmic Star-Formation History, Piero Madau and Mark Dickinson, 2014 (arXiv:1403.0007 [astro-ph.CO])

[7] Kennicutt, R. C. 1983, ApJ, 272,54

[8] G.B. Taylor, C.L. Carilli and R.A. Perley (editors), Synthesis Imaging in Radio Astronomy II, ASP Conference Series, Vol 180, 1999

[9] Schwab, F.R. 1980, Proc. S.P.I.E. , 231 ,18-25.

[10] M. Davis et al., The All-wavelength Extended Groth Strip International Survey (AEGIS) Data Sets, 2006.

[11] Giavalisco, M., et al. 2004, ApJ, 600, L93

[12] Jeffrey A. Newman et al., The DEEP2 Galaxy Redshift Survey: Design, Observations, Data Reduction, and Redshifts, ApJS, 2013.

[13] T. J. Cornwell, K. Golap and S. Bhatnagar, The non-coplanar baselines effect in radio interferometry: The W-projection algorithm, 2008.

[14] Dharam Vir Lal, GMRT Observers Manual, 2013.

[15] Weiner B. J. et al., 2009, ApJ, 692, 187

[16] Mostek N. et al., 2012, ApJ, 746, 124

[17] Willmer C. N. A. et al., 2006, ApJ, 647, 853

[18] White R. L. et al., 2007, ApJ, 654, 99

[19] Noeske K. G. et al., 2007, ApJ, 660, L43

[20] Kobayashi et al., Revisiting the Cosmic Star Formation History, ApJ, Vol 763, No.3, 2013.

[21] Damen M. et al., 2009, ApJ, 690, 937

[22] Gonzalez V. et al., 2014, ApJ, 781, 34

[23] Brinchmann J. et al., 2004, MNRAS, 351, 1151

[24] Salim S. et al., 2007, ApJS, 173, 267

[25] Elbaz D. et al., 2007, AA, 468, 33

[26] Pannella M. et al., 2009, ApJ, 698L, 116

[27] Pannella M. et al., 2015, ApJ, 807, 141

[28] Oteo I. et al., 2014, 439, 1337